# Supplementary material

## Strengthened relaxor behavior in $(1-x)Pb(Fe_{0.5}Nb_{0.5})O_3–xBiFeO_3$

Uroš Prah,[a,b] Mirela Dragomir,[a] Tadej Rojac,[a,b] Andreja Benčan,[a,b] Rachel Broughton,[c] Ching-Chang Chung,[d] Jacob L. Jones,[c] Rachel Sherbondy,[e] Geoff Brennecka[e] and Hana Uršič[a,b,*]

[a] Jožef Stefan Institute, Jamova cesta 39, 1000 Ljubljana, Slovenia.
[b] Jožef Stefan International Postgraduate School, Jamova cesta 39, 1000 Ljubljana, Slovenia.
[c] Department of Materials Science and Engineering, North Carolina State University, Raleigh, NC 27695, USA.
[d] Analytical Instrumentation Facility, North Carolina State University, Raleigh, NC 27695, USA.
[e] Colorado School of Mines, 1500 Illinois St., Golden, CO 80401, USA.
[*] Corresponding author: hana.ursic@ijs.si

## A. XRD analysis of mechanochemically activated powder

The optimal total milling time of mechanochemical activation process of PFN–100xBFO (x = 0.05–0.50) was determined from XRD analysis of powders, which were analyzed after certain time of high-energy milling. XRD patterns of PFN–50BFO powder after certain time of activation are shown in Fig. S1. Similar behavior was also observed in all other PFN–100xBFO (x = 0.05–0.40) compositions.

Initially, during the first 6 h, mainly amorphization of starting oxides takes place, which is reflected in a decrease in the intensity of the diffraction peaks and an increase in the background. Between 6 and 8 h of milling, the perovskite phase begins to form. After 14 h all the starting oxides were transformed either to amorphous or crystalline perovskite phase (approximate mass ratio of 50:50). Because perovskite phase was already formed during the high-energy milling, no additional calcination step before sintering was needed.

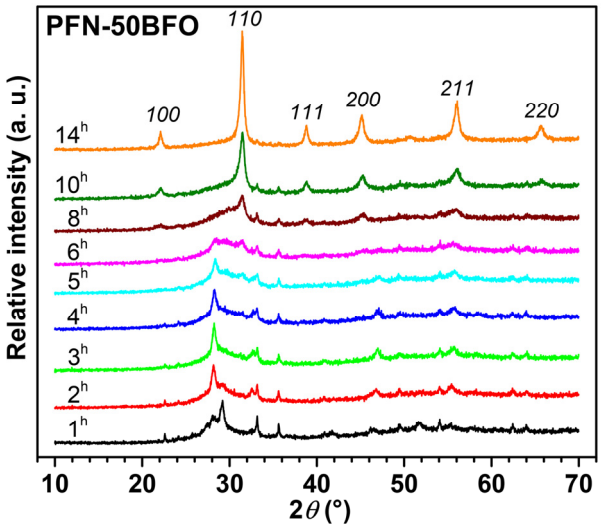


Figure S1. Room-temperature XRD patterns of PFN–50BFO powder after certain time of mechanochemical activation (1–14 h). Diffraction peaks corresponding to perovskite phase are indexed according to the cubic notation.

## B. Sintering behavior of samples

The dynamic sintering curves of the powder compacts were recorded during heating using an optical dilatometer (Leitz Version 1A, Leitz, Wetzlar, Germany). In all cases heating rate of 5 °C·min$^{-1}$, which is the lowest calibrated temperature rate of our instrument, was used. Sintering curves of all PFN–100*x*BFO ($x$ = 0–0.5) solid solutions are shown in Fig. S2. With increasing amount of BFO the densification of the samples, evidenced as a rapid shrinkage of the powder compact, shifts toward lower temperatures.

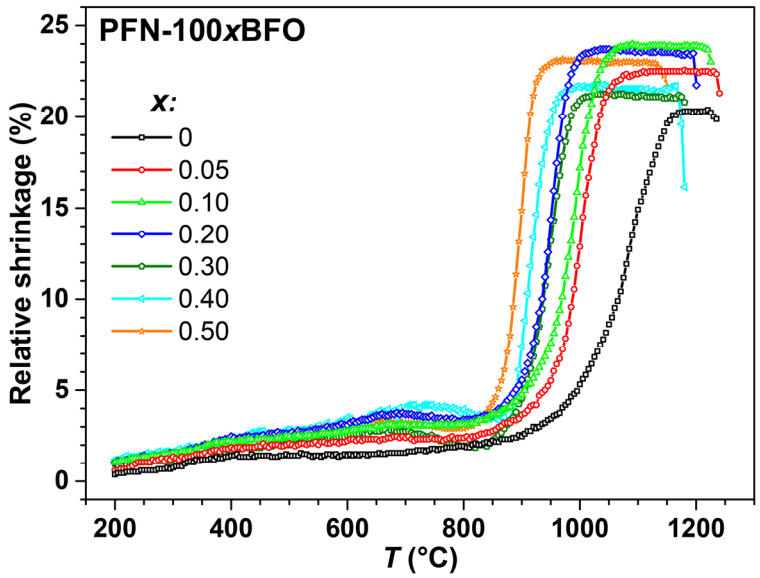


Figure S2. Dynamic sintering curves of different PFN–100*x*BFO ($x$ = 0–0.5) powder compacts.

We point out that for the actual sintering process heating rate of 5 °C·min$^{-1}$ did not result in sufficiently dense ceramics, while prolonged duration time of sintering process led to higher PbO losses and consequently more electrically conductive samples. Therefore, to achieve sufficient densification and at the same time to minimize the evaporation of PbO, the heating rate of 2 °C·min$^{-1}$ was used. Note that due to the use of different heating rates in sintering process and in dynamic sintering curve measurement, the direct comparison of densification process is not possible. The dynamic sintering curves serve only to estimate the approximate sintering temperature.

## C. Microstructure and grain size distributions

SEM images of the thermally etched surfaces and grain size distributions of different PFN–100*x*BFO (x = 0–0.5) solid solutions are shown in Fig. S3. In all compositions, SEM images reveal uniform and dense microstructures (note that in some samples also some pull-outs, produced during the sample surface preparation, are present). In all samples, a unimodal grain size distribution is observed.

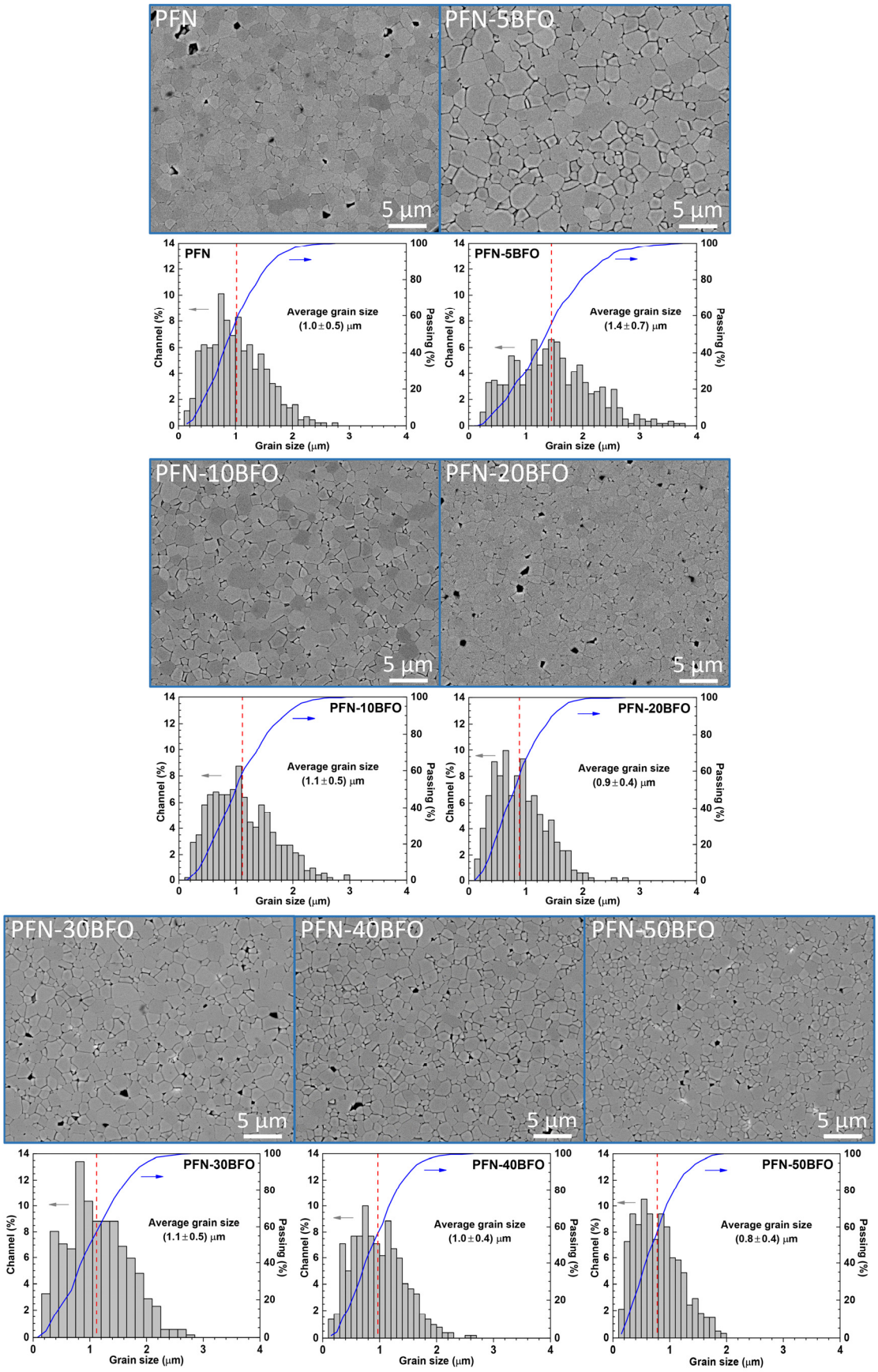


Figure S3. SEM images of thermally etched surfaces and the grain size distributions of different PFN–100*x*BFO (*x* = 0–0.5) solid solutions.

## D. Rietveld refinement

The XRD patterns of crushed PFN–100*x*BFO (*x* = 0–0.5) ceramic pellets are shown in Fig. S4. Only the peaks corresponding to the perovskite phase are observed with no additional secondary phase (see inset of Fig. S4).

The phase composition, crystal structure and lattice parameters of PFN–100*x*BFO (*x* = 0–0.5) were investigated by the Rietveld refinement method. The agreement factors of the Rietveld analysis along with the cell parameters of all the samples are given in Table S1.

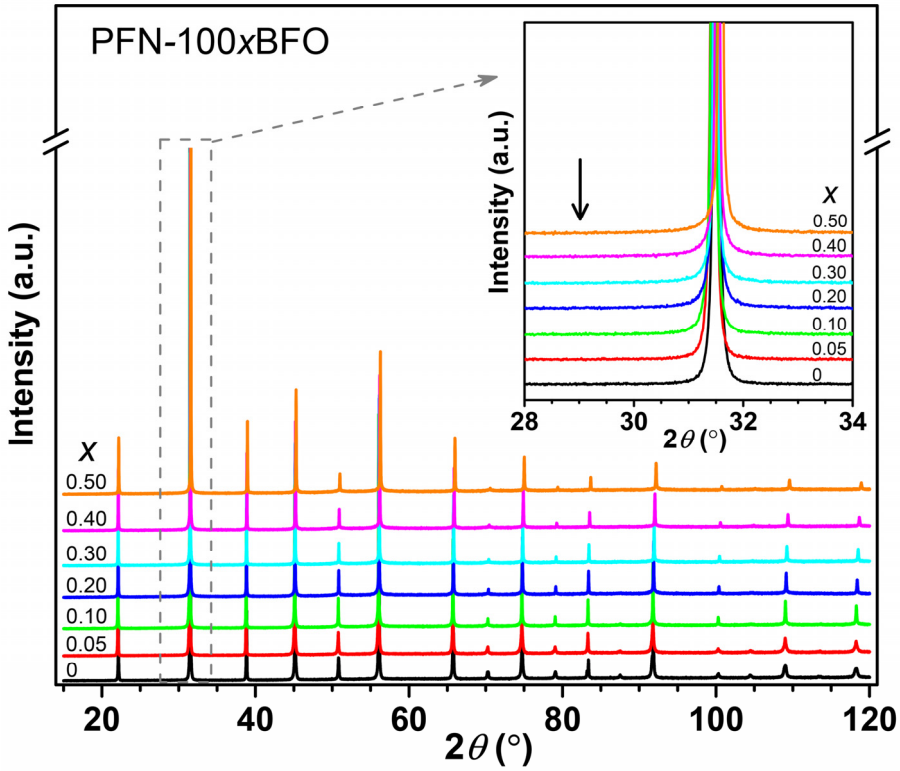


Figure S4. Room-temperature XRD patterns of PFN–100*x*BFO (*x* = 0–0.5) solid solutions. The inset shows an enlarged 2$\theta$ region with an arrow marking the position where the strongest pyrochlore peak would appear.

Table S1: Refined structural parameters for PFN–100$x$BFO ($x$ = 0–0.5) solid solutions.

| Composition | **PFN** | **PFN-5BFO** | | **PFN-10BFO** | | **PFN-20BFO** | **PFN-30BFO** | **PFN-40BFO** | **PFN-50BFO** |
|---|---|---|---|---|---|---|---|---|---|
| Crystal system | Monoclinic | Monoclinic | Cubic | Monoclinic | Cubic | Cubic | Cubic | Cubic | Cubic |
| Space group | *Cm* | *Cm* | *Pm*$\bar{3}$*m* | *Cm* | *Pm*$\bar{3}$*m* | *Pm*$\bar{3}$*m* | *Pm*$\bar{3}$*m* | *Pm*$\bar{3}$*m* | *Pm*$\bar{3}$*m* |
| Weight fraction (%) | 100 | 56.73(5) | 43.27(5) | 12.22(2) | 87.78(2) | 100 | 100 | 100 | 100 |
| $a$ (Å) | 5.67774(7) | 5.67084(9) | 4.01314(2) | 5.66320(6) | 4.01245(2) | 4.01038(9) | 4.00764(1) | 4.00420(4) | 3.99951(6) |
| $b$ (Å) | 5.67196(4) | 5.67056(9) | / | 5.66078(5) | / | / | / | / | / |
| $c$ (Å) | 4.01775(7) | 4.02244(7) | / | 4.02999(3) | / | / | / | / | / |
| $\beta$ (°) | 89.8843(9) | 89.9867(9) | / | 89.5823(8) | / | / | / | / | / |
| $V$ (Å$^3$) | 129.3873(3) | 129.3491(9) | 63.6329(7) | 129.1906(9) | 64.5993(6) | 64.4999(9) | 64.3674(4) | 64.2020(1) | 63.9767(6) |
| $\rho$ (g·cm$^{-3}$) | 8.4595(1) | 8.4619(4) | 8.3768(1) | 8.4724(6) | 8.2565(8) | 8.4123(5) | 8.3727(1) | 8.3509(1) | 8.3368(6) |
| $R_{wp}$ (%) | 7.693 | 7.125 | | 9.837 | | 7.703 | 7.449 | 7.665 | 7.520 |
| $R_{exp}$ (%) | 5.125 | 5.053 | | 4.937 | | 4.931 | 5.054 | 4.997 | 4.866 |
| $R_p$ (%) | 5.644 | 5.374 | | 6.874 | | 5.885 | 5.638 | 5.710 | 5.621 |
| *G. O. F.* | 1.501 | 1.410 | | 1.992 | | 1.562 | 1.474 | 1.534 | 1.545 |
| $R_b$ (%) | 2.399 | 1.636 | 4.736 | 8.161 | 7.816 | 2.456 | 2.123 | 2.696 | 2.895 |

## E. Vogel-Fulcher analysis

The fitting formalism and the adequacy of the data obtained from our setup were first tested on a prototype relaxor material, $Pb(Mg_{1/3}Nb_{2/3})O_3$ (PMN). PMN ceramic was prepared from oxides using mechanochemical-activation-assisted synthesis followed by sintering at 1200 °C for 2 h in the presence of PMN packing powder with the same composition as the pellets. Details of the synthesis procedure are described in Ref. [1].

$T_{e,max}(\omega)$ relations of PMN ceramics were fitted with V-F equation (details can be found in the manuscript), where three V-F parameters were obtained (Fig. S5). The dielectric permittivity data fits well with the V-F law resulting in $\omega_0$, $E_a$ and $T_f$ of ~$3.5 \cdot 10^{14}$ rad·s$^{-1}$, ~0.087 eV and −48 °C, respectively. The results are in a good agreement with literature data.[1-3]

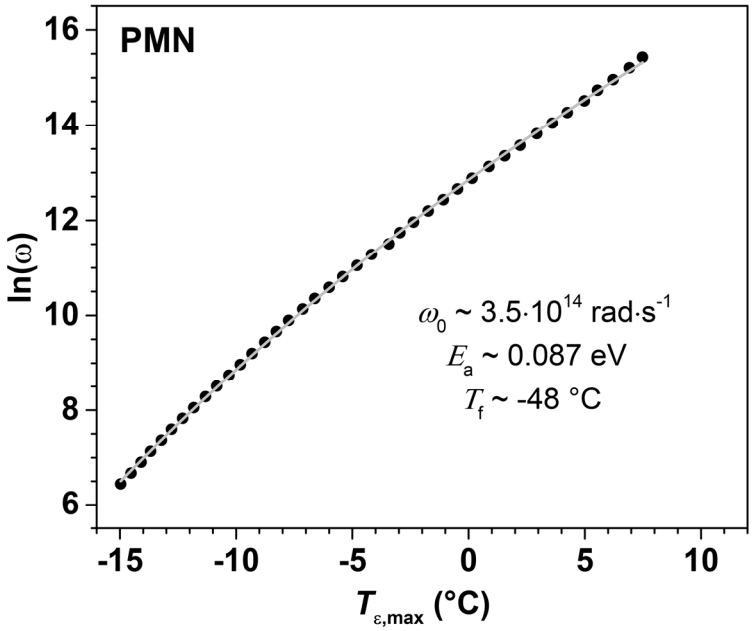


Figure S5. $T_{\varepsilon,max}$ versus ln($\omega$) relation of PMN. Line curve shows the fit of data with V-F equation (see text in the manuscript) from where V-F parameters $\omega_0$, $E_a$ and $T_f$ are obtained.

## F. Differential Scanning Calorimetry

Thermal changes that correspond to structural phase transitions of the ceramic samples were determined from the differential scanning calorimetry curves measured using a differential scanning calorimeter, DSC (Netzsch, DSC 204 F1, Selb, Germany). The measurements were performed on ceramic pellets of ~6 mm in diameter and thickness of ~0.25 mm, which were placed in Pt crucible with lid. In order to eliminate the possible thermal effects related to water evaporation and desorption of gasses from the surface of the sample, two heating and cooling cycles were performed for each composition. In the first cycle, the samples were heated from 25 °C to 500 °C followed by cooling down to −50 °C using liquid nitrogen. Afterwards the samples were heated again to 500 °C followed by cooling back to 25 °C. For all measurements heating and cooling rates of 10 °C·min$^{-1}$ were used.

Temperature dependences of DSC signals of all compositions, obtained from the second heating run, are shown in Fig. S6. In pure PFN an endothermic anomaly at ~100 °C, which according to dielectric permittivity measurements belongs to paraelectric-to-ferroelectric phase transition,

was observed (Fig. S6a). In PFN–100*x*BFO compositions with $x \leq 0.20$ no detectable thermal changes were seen, which is in a good agreement with the nature of canonical relaxor materials, where no structural phase transitions should be present. On the other hand, in compositions with $x \geq 0.30$ (Fig. S6b and c) endothermic anomalies were detected in the vicinity or slightly below the temperatures where the high-temperature anomalies appeared in dielectric permittivity measurements (Fig. 3 in the manuscript). The reason for the difference in the temperature of the anomaly occurrence may be partly due to the different measurement conditions of the both techniques (i.e., different heating/cooling rates, furnace configuration, measurement principle, etc.)

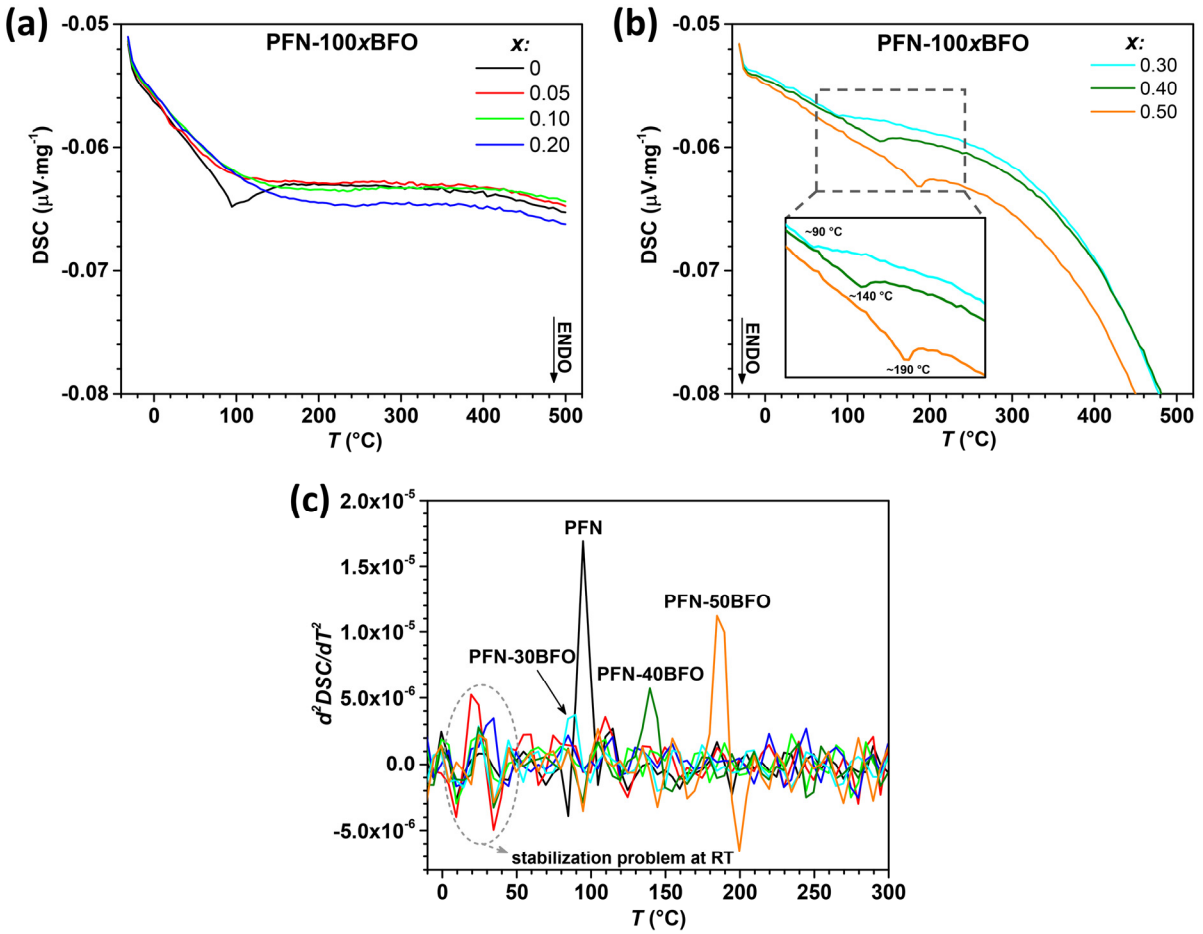


Figure S6. Temperature dependences of DSC signals of (a) $x \leq 0.20$ and (b) $x \geq 0.30$ PFN–100*x*BFO solid solutions. (c) The second derivative of DSC signals of all PFN–100*x*BFO ($x$ = 0–0.5) compositions.

## G. High temperature XRD

High temperature XRD (HT XRD) patterns of PFN–50BFO ceramic pellet were recorded on PANalytical Empyrean X-ray diffractometer (PANalytical B.V., Netherlands) equipped with Cu *Kα* radiation (containing both $K\alpha_1$ and $K\alpha_2$) and a furnace heating stage. Diffraction patterns were recorded in the 15–80° 2$\theta$-range with a step size of 0.013° and an integration time of 100 s per step. The measurements were performed in a temperature range from 25 °C to 300 °C with the step of 25 °C. The phase identification was done with PDF-4+ database. For the

measurements, disk-like shaped ceramic pellet with a diameter of ~14 mm and thickness of ~1 mm were used.

A series of XRD patterns of PFN–50BFO, recorded in a temperature range of 25–300 °C, are shown in Fig. S7. Beside an increase in the lattice parameter (peak shift to lower $2\theta$) due to thermal expansion, there is no other changes in the structure with the temperature. The change of lattice parameters with temperature were additionally investigated by the Rietveld refinement analysis (details in section C), where no specific anomalies were observed (Fig. S8).

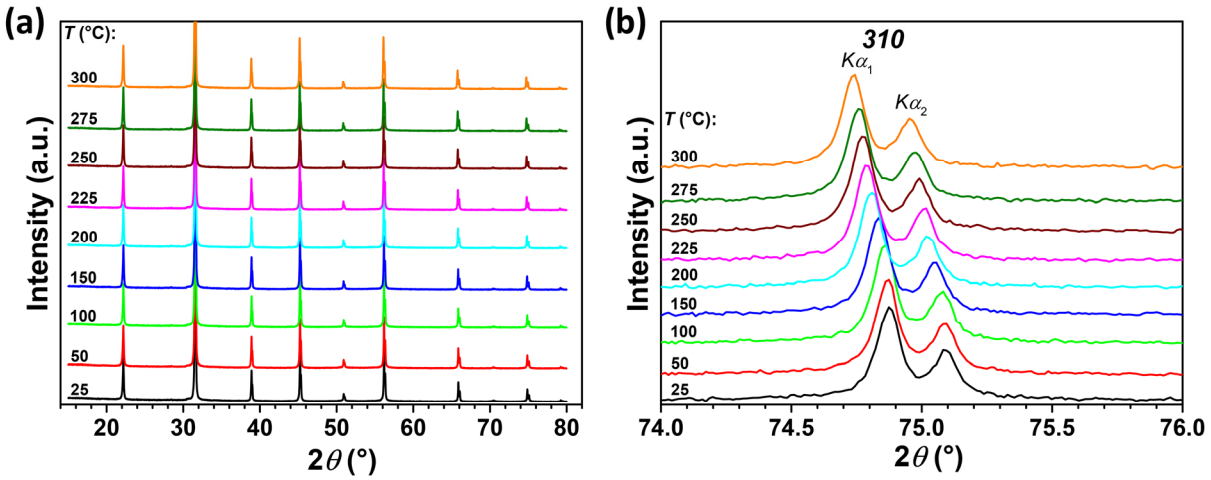


Figure S7. (a) Temperature dependence of XRD patterns of PFN–50BFO with (b) enlarged view of *310* pseudocubic reflection (from Cu $K\alpha_1$ and $K\alpha_2$).

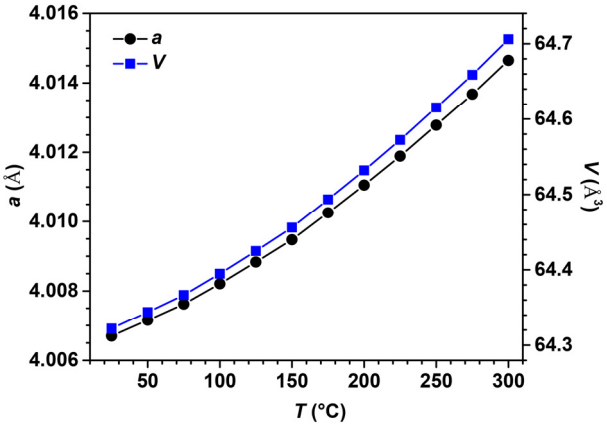


Figure S8. Temperature dependences of lattice parameter and unit cell volume of PFN–50BFO. The blue and black lines are guides to the eye.

## H. High resolution TEM

HRTEM images of PFN–20BFO and PFN–50BFO and corresponding FFTs are shown in Figs. S9a and S9b, respectively. As it can be seen from FFTs, superlattice *½ ½ 0* reflections (α spots) are only observed in the PFN–50BFO sample, which might indicate the existence of antiferroelectric order in the material. As indicated by the inverse FFT image using α spots, nanometer large regions can be found (Fig. S9c). On the other hand, no sign of those spots were seen in PFN–20BFO.

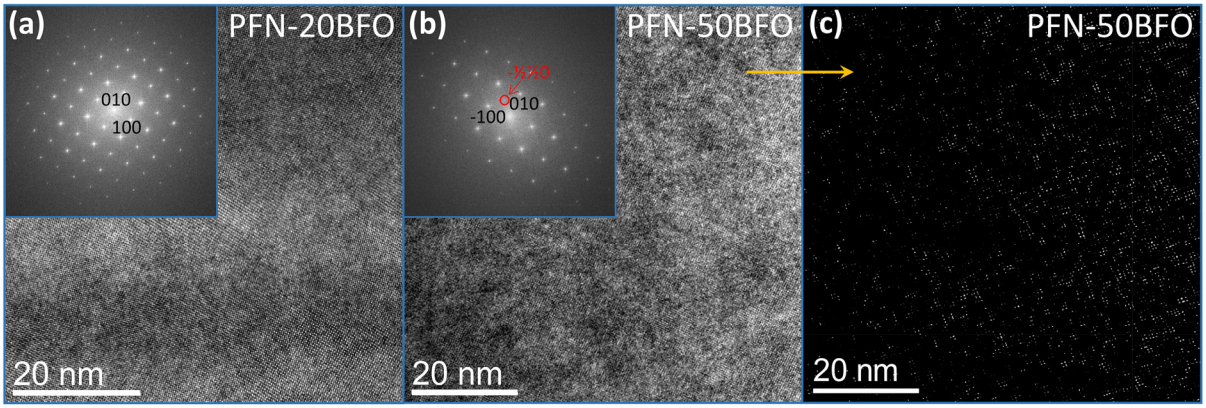


Figure S9. HRTEM images of (a) PFN–20BFO and (b) PFN–50BFO grains in [*001*] zone axis with corresponding FFTs in the insets. The FFT of PFN–50BFO reveals diffuse superlattice *½ ½ 0* spots (marked with red arrow). (c) The inverse FFT image of PFN–50BFO using marked diffuse spots indicates 5 nm large regions.

## I. *S–E* hysteresis loops and *S–P* plots

*S–E* hysteresis loops of PFN–100*x*BFO ($x$ = 0–0.5) compositions are shown in Fig. S10. In pure PFN, ferroelectric butterfly-like hysteresis loops, typically observed due to switching of ferroelastic domain walls in ferroelectric materials,[4] were obtained. With increasing content of BFO up to $x$ = 0.3, the *S–E* loops become slimmer and more quadratic-like indicating increased contribution probably from electrostriction. In $x$ = 0.4 and 0.5 compositions, the *S–E* loops start again to open up and gradually become more hysteretic.

During the *S–E* loop measurements, the *P–E* loops were simultaneously measured. The decreasing piezoelectric response (as shown in Fig. 10 of the main paper) and strengthening of the electrostrictive-like response with increasing amount of BFO in PFN–100*x*BFO solid solutions are also visible from the strain–polarization (*S–P*) plots (Figs. S10). In order to highlight how the electromechanical behavior of the samples deviates from pure electrostrictive response, the *S–P* plots were fitted with quadratic function of the type $S = Q \cdot P^2$, where the fitted parameter $Q$ represents the electrostriction coefficient.[5]

As seen in Fig. S11, in pure PFN, a hysteretic *S–P* response with the largest deviation from the quadratic relation is observed. With increasing content of BFO up to $x$ = 0.2, the hysteresis gradually diminishes and smaller deviation from the pure quadratic response is observed, indicating an increasing contribution of the electrostrictive-like response. In compositions with higher BFO contents ($x \geq$ 0.3), small deviation from pure electrostrictive response is maintained, while the *S–P* response gradually become more hysteretic, which is consistent with the appearance of the pinched *P–E* loops (see Fig. 8 in the main paper).

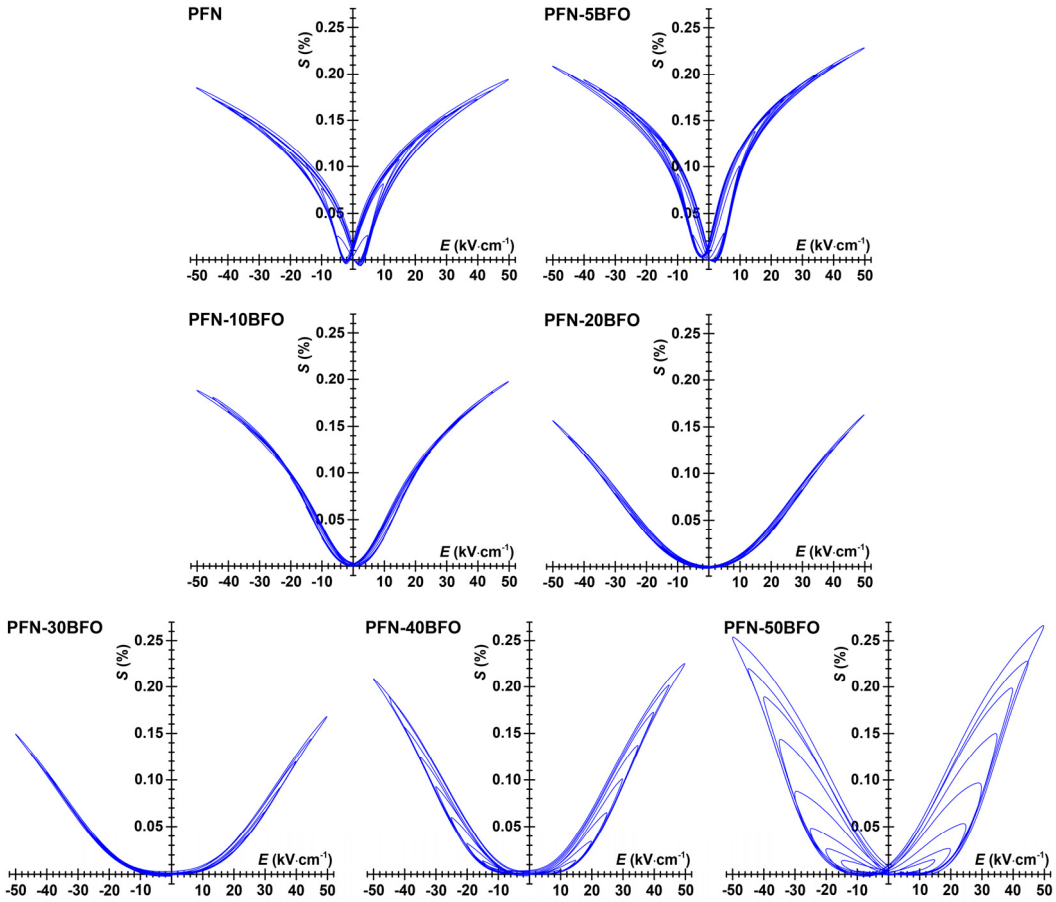


Figure S10. *S*–*E* hysteresis loops of PFN–100*x*BFO (*x* = 0–0.5) at room temperature measured with increasing electric-field amplitude at driving frequency of 10 Hz.

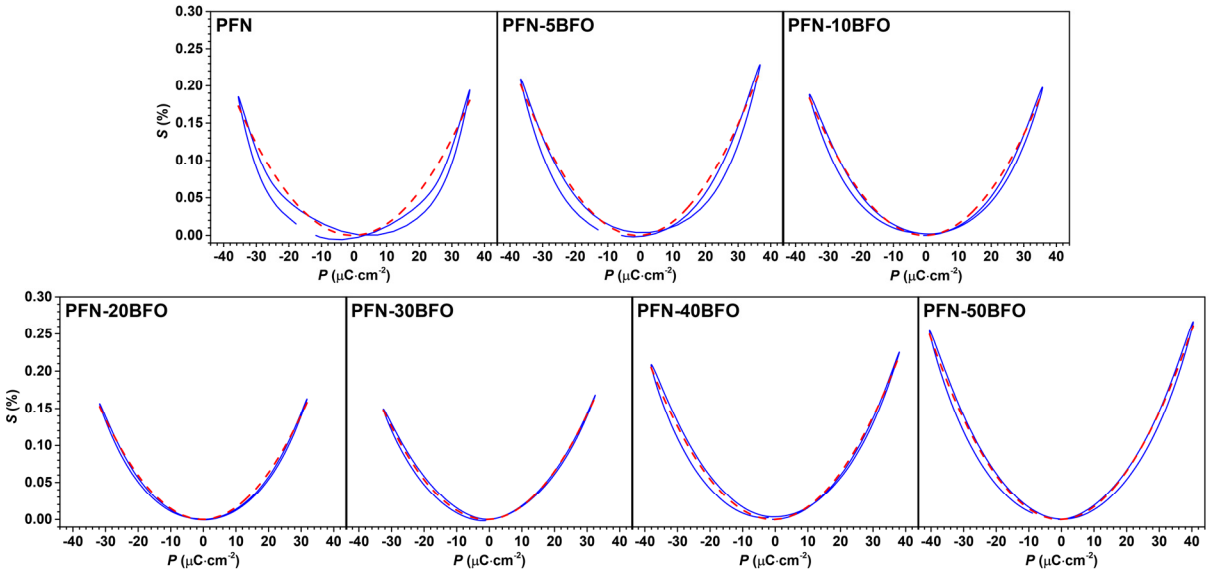


Figure S11. *S*–*P* plots of PFN–100*x*BFO (*x* = 0–0.5) at room temperature shown for 50 kV·cm$^{-1}$ and driving frequency of 10 Hz. With red dashed curve fitted quadratic relation between *S* and *P* are shown.

## J. *J–E* hysteresis loops

*J–E* hysteresis loops of PFN–100*x*BFO (*x* = 0–0.5) compositions are shown in Fig. S12. Pinching of *P–E* hysteresis loops of composition with $x \geq 0.2$ is clearly visible as a splitting of peaks (double current peaks) obtained from *J–E* hysteresis loop measurements (marked by arrows in Fig. S12).

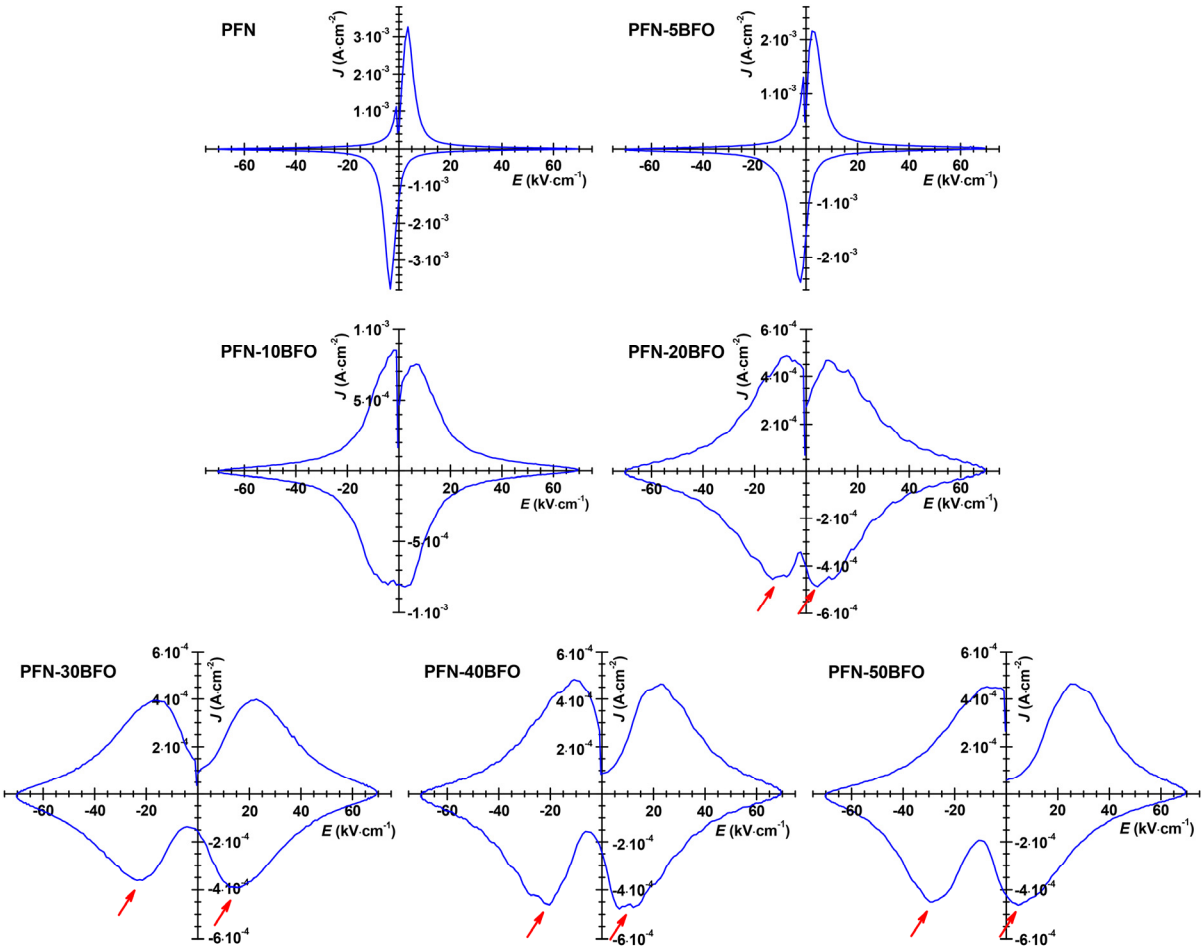


Figure S12. *J–E* hysteresis loops of PFN–100*x*BFO (*x* = 0–0.5) solid solutions measured at room temperature and 70 kV·cm$^{-1}$.

## K. AC electric-field-cycling experiments

In order to investigate the origin of pinching observed in *P–E* measurements, AC electric-field-cycling experiments were performed on a PFN–50BFO sample. The *P–E* loops were continuously measured 50 times at room temperature by applying a single sinusoidal waveform with a frequency and electric field of 1 Hz and 60 kV·cm$^{-1}$, respectively. As can be seen in Fig. S13a, no changes in the shape of the *P–E* loops (i.e., de-pinching) were observed regardless of the cycle number. After cycling, the sample was aged for 1 hour in zero-field conditions and the *P–E* measurement was performed again. As can be seen in Fig. S13b, even after aging experiment, practically no change in the shape of *P–E* loop was observed.

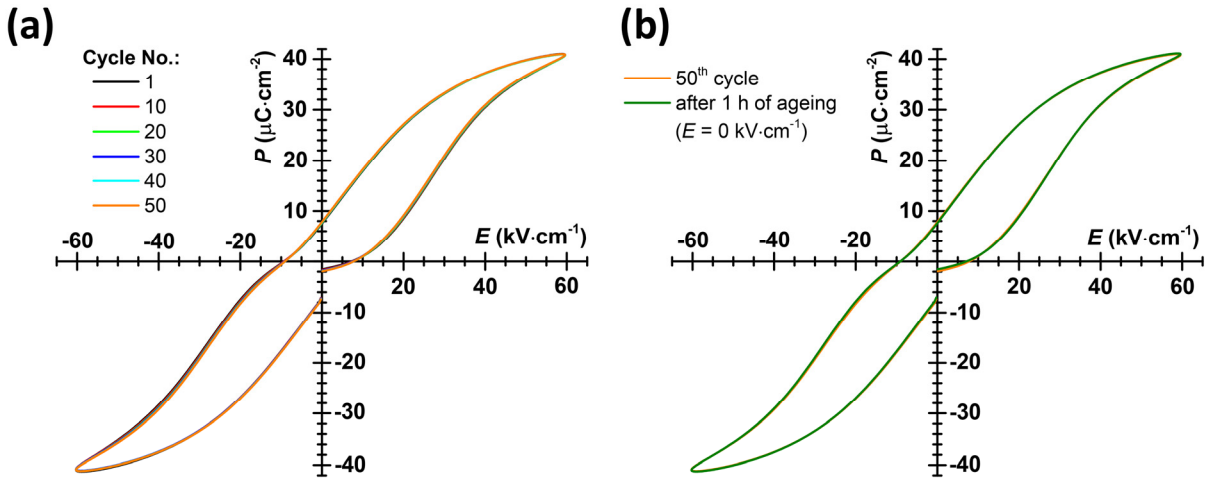


Figure S13. AC electric-field-cycling and aging experiments of PFN–50BFO; (a) The *P*–*E* measurement at 60 kV·cm$^{-1}$ of every tenth cycle. (b) The *P*–*E* measurement after aging compared with the *P*–*E* measurement of 50$^{th}$ cycle.

In order to further investigate the origin of pinching observed in *P*–*E* loops measurements, the measurements of *J*–*E* and *P*–*E* loops at different frequencies were performed. Firstly, the loops were measured at the driving frequency of 10 Hz, where the pinching of the loop was observed (Fig. S14a). In the next step, the driving frequency of the measurement was stepwise reduced from 10 Hz to 0.01 Hz by performing one cycle at each frequency, i.e., 1, 0.1 and 0.01 Hz. During this experiment, performed at low driving frequency, the defects may in principle migrate due to the longer period under the electric field; this is seen in the larger contribution of the electrical conductivity of the material resulting in rounded and leaky *P*–*E* hysteresis loop (Fig. S14a). Finally, after the cycles performed at low frequencies, the driving frequency was increased back to 10 Hz. In principle, if the defects redistribution (migration) under the low-frequency field has any role in the original pinched shape, measured at 10 Hz, the low frequency driving should affect this pinched shape measured at 10 Hz. Only a slight change in the loop shape was observed at 10 Hz after the low-frequency cycles, relative to the first measured 10 Hz loop (see Fig. S14a). This is also seen in the *J*–*E* loops, where little changes are observed between the first and last 10 Hz cycle (compare black and dashed orange loops in Fig. S14b).

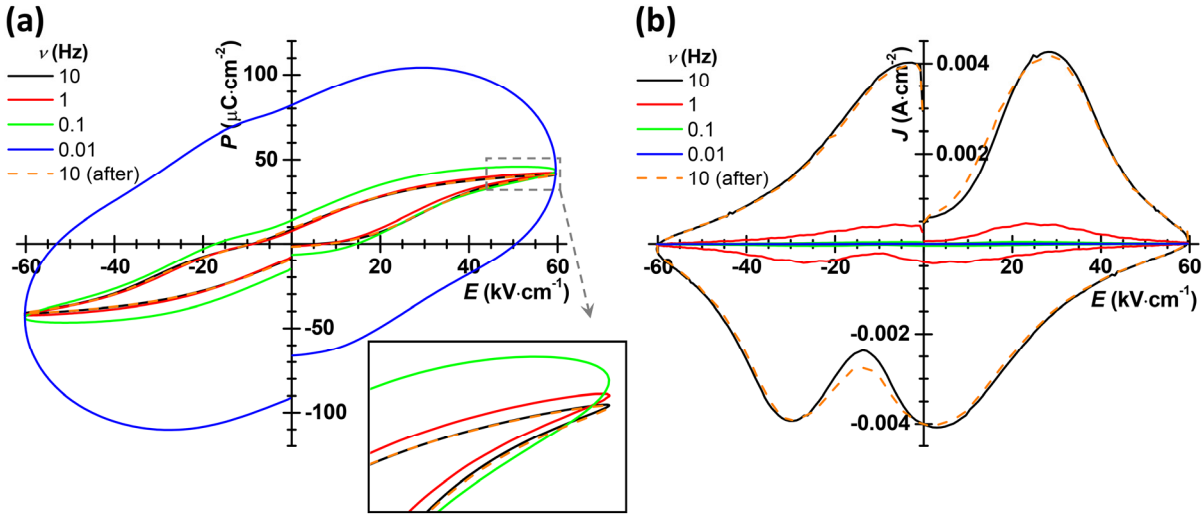


Figure S14. (a) *P–E* and (b) *J–E* hysteresis loops of PFN-50BFO measured at 60 kV·cm$^{-1}$ using different driving frequencies at room temperatures.

## L. Rapid cooling (quenching) experiment

The role of charged defects on pinching of *P–E* loop was additionally investigated by controlling the post-sintering heat-treatment cooling rate. Distribution of defects can be controlled by the processing cooling rate, namely, quenching from above the Curie temperature induces defect disorder, while slow cooling favors defect ordering. Ideally, in the former the loops should be completely open up, while in the latter should be pinched (if defect distribution has any role in the pinching behavior).[6]

In this experiment, first, the thinned (~200 μm) PFN-50BFO ceramic pellet was heated to 600 °C for 1 h and then slowly cooled down to room temperature with the cooling rate of 1 °C·min$^{-1}$ (named as non-quenched sample). The surfaces of the pellets were coated with Au electrodes and the *J–E* and *P–E* loops were obtained at 1 Hz and 60 kV·cm$^{-1}$. After that, the same pellet was heated to 400 °C for 5 min and immediately cooled down by quenching in water (quenched sample). The measurement of *J–E* and *P–E* loops were repeated using the same measurement conditions.

The *J–E* and *P–E* loops of both experiments are shown in Fig. S15. Compared to the non-quenched sample, the degree of pinching was slightly decreased when the sample was quenched. Small difference in *J–E* and *P–E* responses of the sample exposed to different cooling rates show that the ordering of charged defects can be partially responsible for the pinching of the loop.

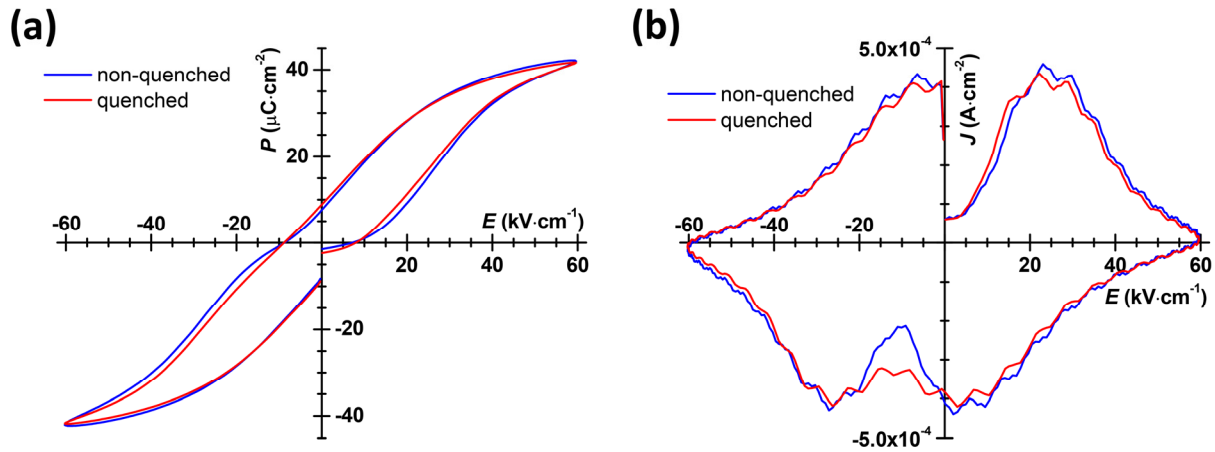


Figure S15. (a) *P*–*E* and (b) *J*–*E* hysteresis loops of PFN-50BFO measured after slowly (1 °C·min$^{-1}$) and rapid cooling of sample.

## M. *in situ* sXRD

*In situ* sXRD measurements of PFN–40BFO were employed. Maps of the *111* and *200* pseudocubic reflections during *in situ* applied voltage up to 50 kV·cm$^{-1}$ and after release are shown in Fig. S16. In contrast to PFN–50BFO, the electric-field-induced phenomenon, namely the broadening and weakening in peak intensity parallel to the field is substantially less pronounced.

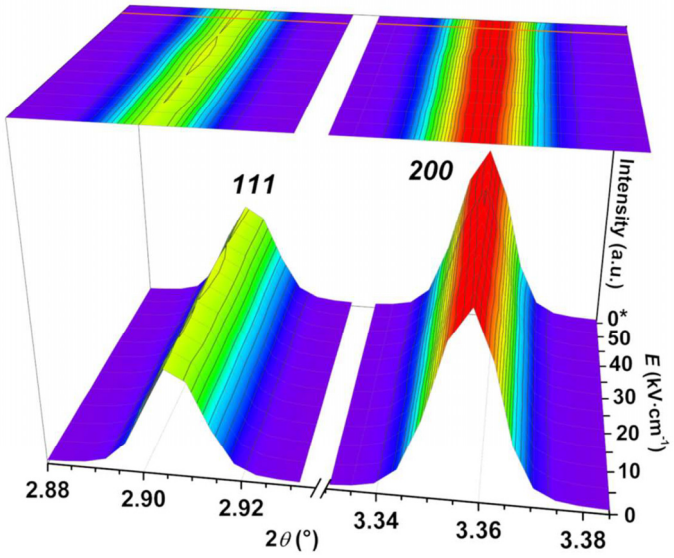


Figure S16. Room-temperature *in situ* sXRD surface contour plots of the (a) *111* and (b) *200* pseudocubic reflections of PFN–40BFO with *in situ* applied voltage up to 50 kV·cm$^{-1}$ and after release (*0 kV·cm$^{-1}$).

# References

[1] H. Ursic and D. Damjanovic, *Appl. Phys. Lett*., 2013, **103**, 072907 1–4.
[2] A. E. Glazounov and A. K. Tagantsev, *Appl. Phys. Lett*., 1998, **73**, 856–858.
[3] D. Viehland, S. J. Jang, L. E. Cross and M. Wuttig, *J. Appl. Phys*., 1990, **68**, 2916–2921.
[4] D. Damjanovic, *Rep. Prog. Phys.*, 1998, **61**, 1267–1324.
[5] S. Nomura and K. Uchino, *Ferroelectrics*, 1982, **41**, 117–132.
[6] D. Damjanovic, in *The Science of Hysteresis*, eds. I. Mayergoyz and G. Bertotti, Elsevier, Volume 3, 2006, Chapter 4, 337–465.